



Rubbing dynamic characteristics of the blisk-casing system with elastic supports

Jin Zeng^a, Chenguang Zhao^a, Hui Ma^{a,b,*}, Kun Yu^a, Bangchun Wen^a

^a School of Mechanical Engineering and Automation, Northeastern University, Shenyang, Liaoning 110819, PR China

^b Key Laboratory of Vibration and Control of Aero-Propulsion System Ministry of Education, Northeastern University, Shenyang, Liaoning 110819, PR China

ARTICLE INFO

Article history:

Received 26 August 2019
Received in revised form 11 October 2019
Accepted 12 October 2019
Available online xxxx

Keywords:

Multi-blades
Flexible casing
Rubbing dynamics
Lagrange multiplier method
Craig-Bampton method

ABSTRACT

In order to simulate the rubbing dynamics of the multi-blades/flexible casing, the finite element model (FEM) of the blisk-oval casing system with elastic supports is established using the self-programmed beam-shell-spring hybrid elements in combination with two types of self-programmed interfacial coupling elements (ICEs). The rotating effects such as centrifugal stiffening, spin softening and Coriolis effects for the blade and gyroscopic effect for the disk are all included in the system. For improving the computational efficiency, a two-step hybrid Craig-Bampton method is utilized to build the reduced blisk model and one step reduction for the casing is sufficient. Corresponding accuracy is verified via the frequency convergence analysis. Then the central difference method in combination with the Lagrange multiplier method is applied to solve the rubbing dynamic responses of the reduced system under different rotating speeds and supporting stiffness. The results show that (1) the Craig-Bampton method is appropriate for reducing the number of dimensions and improving the computational efficiency under the premise of ensuring model accuracy; (2) the fundamental frequency in the vibration responses of the casing is the product of the rotating frequency of the blisk and the number of contact zone on the casing, and period-1 motion/chaotic motion indicates the equal/unequal and radially symmetric contact zones on the casing, respectively; (3) the effects of the casing supporting stiffness on the rubbing characteristics of the system are more significant than those of the blisk supporting stiffness, and the vibration responses of the casing relative to the blisk are more sensitive to the system state variations like the occurrence of the resonance.

© 2019 Elsevier Masson SAS. All rights reserved.

1. Introduction

A bladed disk assembly is widely used in the fan, compressor and turbine sections of a gas turbine engine [1]. With the development of the aviation industry, the blade integrated disk, i.e. the blisk, is increasingly popular with the engine designers due to its improvement in the designs for structure simplification, light-weighting and aerodynamic efficiency [2–6]. The researches in Refs. [7,8] indicate that the decreasing clearance between the blade tip and the casing is very helpful to reduce fuel-consumption and tip leakage flow thus improving the engine performance. However, this strategy also brings about the very high likelihood of blade tip-casing rubbing. Additionally, some potential malfunctions [9–13] such as mass eccentricity and mistuning can significantly enlarge the forced response levels of the bladed disk, and then exacerbate the rubbing threat. In Ref. [14], it has been clearly pointed out that the rubbing between the blade tip and the casing is more dangerous than that occurring at seals. Therefore, it is essential to carry out the study on the blade tip-casing rubbing dynamics.

Numerous literatures on the blade tip-casing rubbing have been published and are mainly divided into three categories in terms of their differences in the system modeling: (1) single blade-casing coupled rubbing system [15], (2) bladed disk-casing coupled rubbing system [16], (3) shaft-bladed disk-casing coupled rubbing system [17]. As for (1) single blade-casing coupled rubbing system, a straight cantilevered blade established by the Euler-Bernoulli beam theory is commonly presupposed and only in-plane motion are considered in most cases, while the casing is simulated via either point mass [12,13] or flexible ring [14,15] models. In addition, some scholars also

* Corresponding author at: School of Mechanical Engineering and Automation, Northeastern University, Shenyang, Liaoning 110819, PR China.

E-mail address: mahui_2007@163.com (H. Ma).

adopt semi-analytical [18,19] or finite element [20,21] methods to establish corresponding two- or three-dimensional system models with rub-impact. Even if some rubbing characteristics between the blade tip and the casing can be revealed from this simple system to some extent, corresponding disadvantages are that there is only one definite blade at most interacting with the casing at an arbitrary moment [22–28], which may be impractical in most cases for the industrial engine [29–32]. Relative to (1) single blade-casing coupled rubbing system [33], (2) bladed disk-casing coupled rubbing system is a better substitute especially in simulating the multi-blade tips-casing rubbing characteristics [34]. Various bladed disk-casing coupled dynamic models have been proposed by many scholars [34–38]. Among these papers, there are two major concerns: one is the containment analysis [34,35], and the other is the rubbing-induced complicated dynamic responses [36–38]. For the former, the emphasis is placed on whether the casing suffers from the impact of the high-speed broken blade. This type of rubbing is accompanied by short-lasting duration and material time-varying and damaging behaviors, and the structural strength of the components is the focus of interest. Corresponding numerical simulation and experimental testing are time-consuming, high costs but necessary [34]. For the latter, the material properties of the blade, the disk, and the casing components are usually assumed to be isotropic and linear-elastic, and various model-reduction techniques can be utilized to improve the computational efficiency [38]. Relative to the former rubbing, this type of rubbing is equipped with long action time and rich fault characteristics, which are very suitable for the studies on fault mechanism and feature extraction [39]. However, it should be pointed out that the disk is often assumed to be rigid in the latter concern [40]. Based on (2) bladed disk-casing coupled rubbing system, the shaft is further involved in the system thus turning into (3) shaft-bladed disk-casing coupled rubbing system [41,42]. Under the premise of prohibiting model reduction, it is a common practice to utilize point mass-beam hybrid model [43] to establish the system dynamic model due to the higher computational efficiency and lower memory usage than the other models such as point mass-shell hybrid [44], beam-shell hybrid [45], shell-solid [40] and full solid [46]. In terms of the point mass-beam hybrid model, the shaft and disk are mainly simulated by the beam and point-mass models, respectively [47]; the casing is primarily simulated by point mass [48], hollow beam [49] and flexible ring models [50]; the blade is mostly simulated by either the rigid body model [51] or flexible beam model [52]. Obviously, the flexible beam model [53] has more advantages in simulating the complicated dynamic behaviors of the blade but also causes a larger solution size and a lower computational efficiency than the rigid body model [54]. In addition, some experimental models on blade tip-casing rubbing are also proposed by many scholars [55–57].

The literature survey listed above indicates that lots of researches on blade tip-casing rubbing have been done by many scholars. However, there still exist the following disadvantages especially for considering the effect of the disk: (i) the flexibility and the varying thickness of the disk are less involved; (ii) the non-uniform and pre-twisted cross-section feature of the blade established by the beam theory is less covered; (iii) rotating effects such as gyroscopic effect for the axisymmetric components (e.g. the shaft and the disk) and Coriolis, centrifugal stiffening and spin softening effects for the blade are less fully included into the system. In order to make up the existing deficiencies, the bladed disk-oval casing coupled system with elastic supports is taken as an example, whose finite element model (FEM) is built via the self-programmed beam-shell-spring hybrid elements and two types of the interfacial coupling elements (ICEs). Then a two-step hybrid Craig-Bampton method for the blisk reduction and one reduction for the casing are adopted to establish the reduced blisk-casing system, and corresponding effectiveness is verified via the frequency convergence analysis. Next, the central difference method combining with the Lagrange multiplier method is adopted to solve the rubbing characteristics of the reduced system under different rotating speeds. Finally, some conclusions are made.

2. FEM of the reduced blisk-casing system

Due to the thin-walled design, the casing configuration affected by manufacturing imperfections, in-take flow aerodynamic loads, thermal gradients and mounting conditions should be oval rather than circular [27,28,37,58]. Based on this, the blisk-oval casing system with elastic supports is pre-supposed in this paper, and corresponding three-dimensional (3D) model is shown in Fig. 1(a), which is divided into the three components such as the disk, the blade group, and the casing. In the figure, the disk center O_d is supported by three linear ($k_{d,x}$, $k_{d,y}$ and $k_{d,z}$) and three torsional ($k_{d,rot X}$, $k_{d,rot Y}$ and $k_{d,rot Z}$) springs, and connected to the inner hole of the disk via the rigid zone (see Fig. 1(b)), while the casing is supported by a series of radial ($k_{c,ri}$) and circumferential ($k_{c,ti}$) linear springs (see Fig. 1(b)). Here, it should be noted that only the in-plane motions (XOY plane) of the casing are considered.

In terms of Fig. 1(a), corresponding FEMs are then established (see Fig. 1(b)). Here, the disk is discretized via self-programmed eight-node Mindlin-Reissner shell element (see Refs. [59,60]), while the blade and the casing are discretized via self-programmed two-node Timoshenko beam element (see Ref. [61]). More detailed information on deriving corresponding element matrices can refer to Refs. [59–61], and no further explanations are presented here for the sake of space limitations. Particularly, during the establishment of the FEM of the blisk, there exist two types of crucial couplings such as disk center-inner hole of the disk (see rigid zone in Fig. 1(b), zero dimensional (0D)-two dimensional (2D) coupling) and disk-blade (see Fig. 1(b), 2D-one dimensional (1D) coupling). Unfortunately, less information on dealing with such couplings is elaborated in the existing literatures. Based on this, emphasis will be firstly placed on dealing with these two couplings.

2.1. Disk center-inner hole of the disk ICE

In fact, the coupling between the disk center O_d and the inner hole of the disk is the rigid surface constraint. Taking the i th node pair O_d-i as an example (see Fig. 2), corresponding displacement constraint equations in XOY, YOZ and ZOX are unified as follows:

$$\begin{cases} T_{R,i} \mathbf{q}_i = \mathbf{0} \\ T_{R,i} = \begin{bmatrix} 1 & 0 & 0 & 0 & 0 & 0 & -1 & 0 & 0 & 0 & 0 & Y_i \\ 0 & 1 & 0 & 0 & 0 & 0 & 0 & -1 & 0 & 0 & 0 & -X_i \\ 0 & 0 & 1 & 0 & 0 & 0 & 0 & 0 & -1 & -Y_i & X_i & 0 \\ 0 & 0 & 0 & 1 & 0 & 0 & 0 & 0 & 0 & -1 & 0 & 0 \\ 0 & 0 & 0 & 0 & 1 & 0 & 0 & 0 & 0 & 0 & -1 & 0 \\ 0 & 0 & 0 & 0 & 0 & 1 & 0 & 0 & 0 & 0 & 0 & -1 \end{bmatrix} \end{cases} \quad (1)$$

where $\mathbf{q}_i = [u_i, v_i, w_i, \theta_{i,x}, \theta_{i,y}, \theta_{i,z}, u_{O_d}, v_{O_d}, w_{O_d}, \theta_{O_d,x}, \theta_{O_d,y}, \theta_{O_d,z}]^T$.

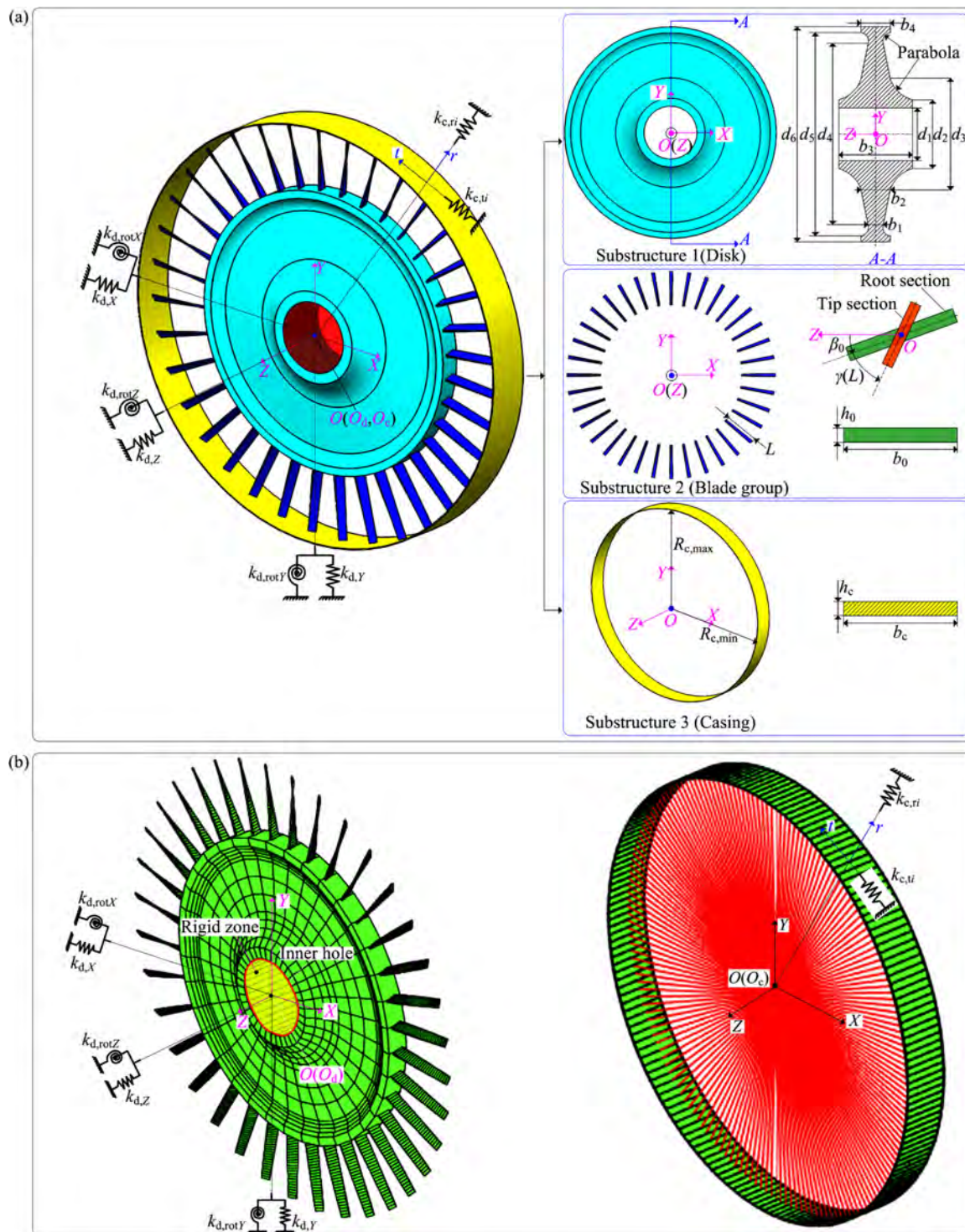


Fig. 1. Bisk-casing system with elastic supports: (a) three-dimensional (3D) model, (b) FEM. (For interpretation of the colors in the figure(s), the reader is referred to the web version of this article.)

Based on Eq. (1), the penalty method is applied to obtain the rigid-coupled stiffness matrix $\mathbf{K}_{rigid}^i = k_p \mathbf{T}_{R,i}^T \mathbf{T}_{R,i}$ of the i th node pair. $k_p = \max(\text{diag}(\mathbf{K}_{d,e}))$ is the penalty term, and $\mathbf{K}_{d,e}$ is the structural stiffness matrix of the disk. Then the global constraint stiffness matrix $\mathbf{K}_{rigid} = \sum_{i=1}^{N_I} \mathbf{K}_{rigid}^i$ can be determined, and N_I represents the node number of the inner hole of the disk.

2.2. Disk-blade ICE

The mass, gyroscopic and structural stiffness matrices of the disk are established in $OXYZ$, while the blade with additional centrifugal stiffening, spin softening and Coriolis matrices included are built in the local co-ordinate system $o_k x_k y_k z_k$ in Fig. 3. Here, the subscript k

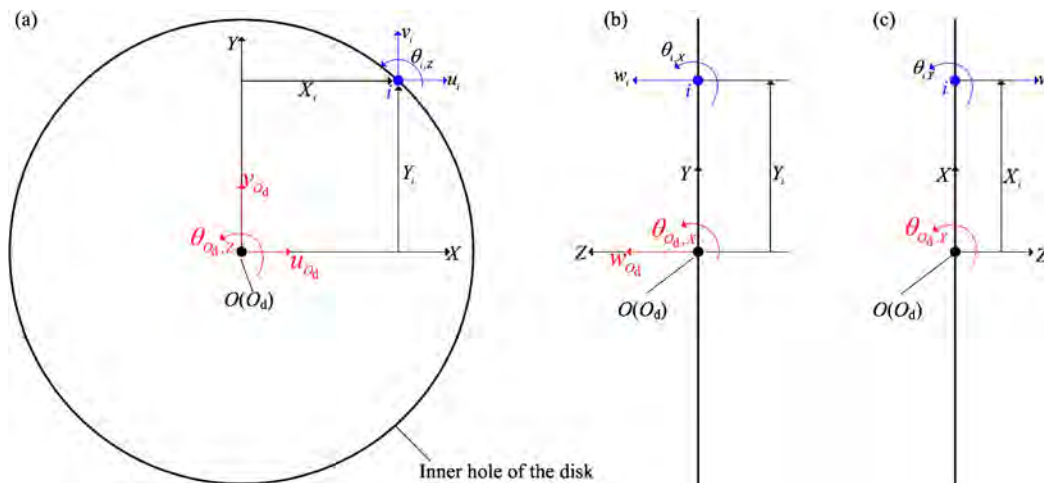


Fig. 2. Displacement compatibility: (a) XOY, (b) YOZ, (c) ZOX.

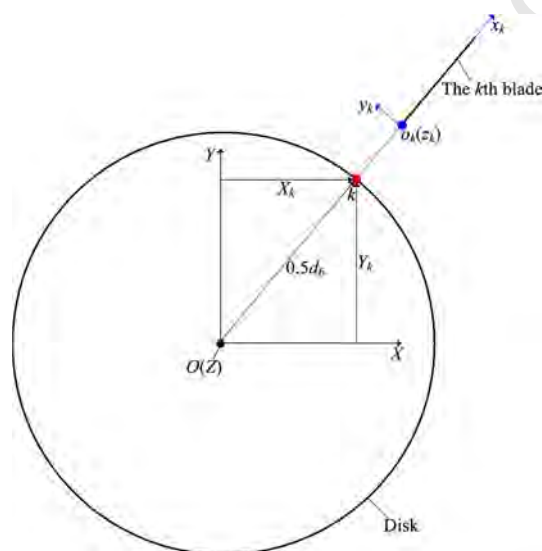


Fig. 3. Relationship between OXYZ and $o_kx_ky_kz_k$.

represents the k th blade. When assembling those matrices of the blade and the disk, the interface displacement compatibility between the outer master nodes of the disk and the root master nodes of the blade should be satisfied.

Taking the coupling between the disk and the k th blade as an example, the transformation matrix from $o_kx_ky_kz_k$ to OXYZ is as follows:

$$\mathbf{T}_k = \frac{2}{d_6} \begin{bmatrix} X_k & -Y_k & 0 & 0 & 0 & 0 \\ Y_k & X_k & 0 & 0 & 0 & 0 \\ 0 & 0 & 1 & 0 & 0 & 0 \\ 0 & 0 & 0 & X_k & -Y_k & 0 \\ 0 & 0 & 0 & Y_k & X_k & 0 \\ 0 & 0 & 0 & 0 & 0 & 1 \end{bmatrix} \quad (2)$$

In light of the displacement compatibility, the displacement constraint equations of the k th ICE in OXYZ can be expressed as follows:

$$[\mathbf{I}_{6 \times 6} \quad -\mathbf{T}_k] \cdot \mathbf{q}_k = \mathbf{0} \quad (3)$$

where $\mathbf{q}_k = [u_{X,k}, v_{Y,k}, w_{Z,k}, \theta_{X,k}, \theta_{Y,k}, \theta_{Z,k}, u_{x_k,o_k}, v_{y_k,o_k}, w_{z_k,o_k}, \theta_{x_k,o_k}, \theta_{y_k,o_k}, \theta_{z_k,o_k}]^T$.

The penalty method is then adopted to obtain the stiffness matrix of the k th ICE $\mathbf{K}_{db}^k = k_p [\mathbf{I}_{6 \times 6} - \mathbf{T}_k]^T \cdot [\mathbf{I}_{6 \times 6} - \mathbf{T}_k]$. The total stiffness matrix of all the ICEs between the disk and the blades $\mathbf{K}_{db} = \sum_{k=1}^{N_b} \mathbf{K}_{db}^k$ can be determined, and N_b represents the blade number.

2.3. Contact strategy

2.3.1. Determination of the contact pairs (CPs)

The Lagrange multiplier method (LMM) is adopted to simulate the interaction process between the multi-blade tips and the casing. The key issue to use the LMM is the establishment of the contact constraint matrices in the normal-, circumferential- and axial-directions. Before deriving these contact constraint matrices, the primary task is to judge which casing segment contacting with which blade tip.

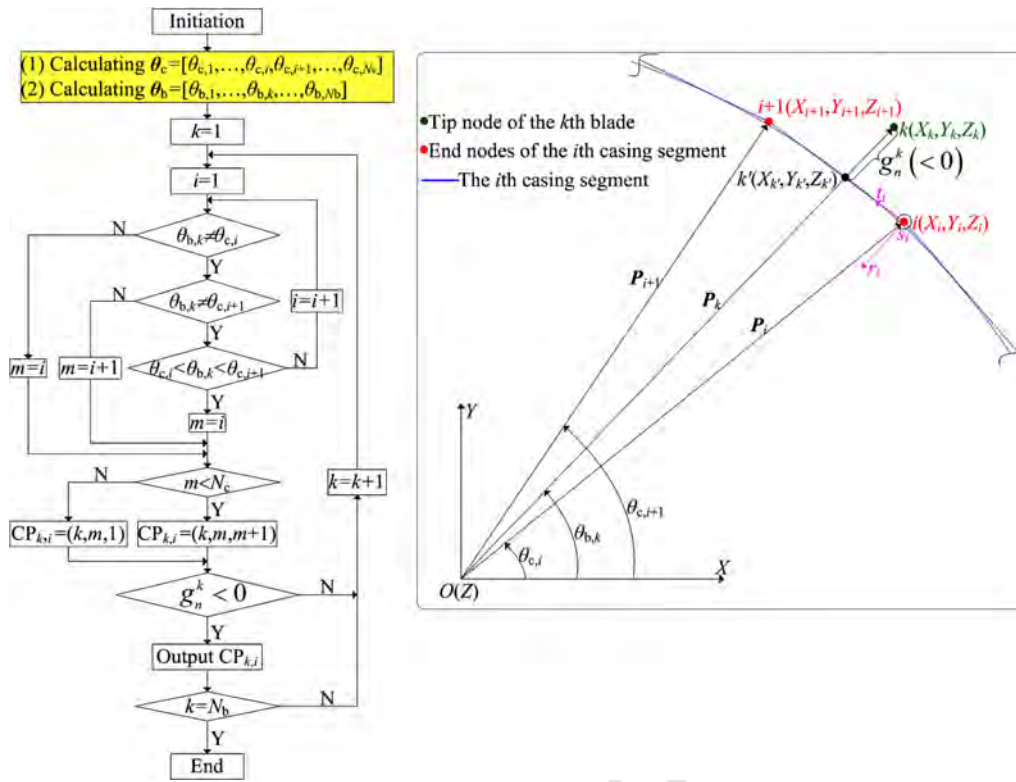


Fig. 4. Contact judgment between the multi-blade tips and the casing.

Taking the k th blade tip and the i th casing segment as an example, the phase angles $\theta_{c,i}$, $\theta_{b,k}$, $\theta_{c,i+1}$ satisfying $\theta_{c,i} \leq \theta_{b,k} \leq \theta_{c,i+1}$ and the contact gap $g_n^k < 0$ in Fig. 4 indicate that the contact between the blade tip of the k th blade and the i th casing segment $i - (i + 1)$ occurs. The flow chart on the contact judgment between the multi-blade tips and the casing is shown in Fig. 4. Here, it should be pointed out that the detailed calculations of $\theta_{c,i}$ and $\theta_{b,k}$ in Fig. 4 can refer to Ref. [62].

2.3.2. Establishment of the contact constraint matrices

Frictionless or frictional status between the blade tip and the casing may exist under the existence of the normal rubbing force. Especially for the frictional status, the friction force is assumed to be a sliding one in this paper.

(1) *Contact constrained matrix in the normal direction* The k th blade contacting with the i th casing segment is taken as an example. Corresponding contact unit vectors \mathbf{r}_i , \mathbf{t}_i , and \mathbf{s}_i are defined as follows:

$$\mathbf{r}_i = (\mathbf{P}_{i+1} - \mathbf{P}_i) / \|\mathbf{P}_{i+1} - \mathbf{P}_i\|, \quad \mathbf{s}_i = [0, 0, 1] \quad \mathbf{t}_i = \mathbf{s}_i \times \mathbf{r}_i \quad (4)$$

Letting $\xi_k = \text{dot}(\mathbf{P}_k - \mathbf{P}_i, \mathbf{t}_i) / \|\mathbf{P}_{i+1} - \mathbf{P}_i\|$, the co-ordinates of k' in OXY can be calculated as follows:

$$\begin{cases} \begin{bmatrix} X_{k'} \\ Y_{k'} \end{bmatrix} = (1 - \xi_k) \begin{bmatrix} X_{i,0} \\ Y_{i,0} \end{bmatrix} + \xi_k \begin{bmatrix} X_{i+1,0} \\ Y_{i+1,0} \end{bmatrix} + \begin{bmatrix} \beta_{k,1}^T \\ \beta_{k,2}^T \end{bmatrix} [u_i, v_i, \varphi_i, u_{i+1}, v_{i+1}, \varphi_{i+1}]^T \\ \beta_{k,1} = \begin{bmatrix} n_{i,x}^2 N_{v1}(\xi_k) + t_{i,x}^2 N_{u1}(\xi_k), n_{i,x} n_{i,y} N_{v1}(\xi_k) + t_{i,x} t_{i,y} N_{u1}(\xi_k), n_{i,x} N_{v2}(\xi_k), \\ n_{i,x}^2 N_{v3}(\xi_k) + t_{i,x}^2 N_{u2}(\xi_k), n_{i,x} n_{i,y} N_{v3}(\xi_k) + t_{i,x} t_{i,y} N_{u2}(\xi_k), n_{i,x} N_{v4}(\xi_k) \end{bmatrix}^T \\ \beta_{k,2} = \begin{bmatrix} n_{i,x} n_{i,y} N_{v1}(\xi_k) + t_{i,x} t_{i,y} N_{u1}(\xi_k), n_{i,y}^2 N_{v1}(\xi_k) + t_{i,y}^2 N_{u1}(\xi_k), n_{i,y} N_{v2}(\xi_k), \\ n_{i,x} n_{i,y} N_{v3}(\xi_k) + t_{i,x} t_{i,y} N_{u2}(\xi_k), n_{i,y}^2 N_{v3}(\xi_k) + t_{i,y}^2 N_{u2}(\xi_k), n_{i,y} N_{v4}(\xi_k) \end{bmatrix}^T \end{cases} \quad (5)$$

where $\mathbf{N}_v = [N_{v1}(\xi_k), N_{v2}(\xi_k), N_{v3}(\xi_k), N_{v4}(\xi_k)]^T$ and $\mathbf{N}_u = [N_{u1}(\xi_k), N_{u2}(\xi_k)]^T$ are the displacement interpolation functions in the flexural and axial directions, respectively [61,63]; $(n_{i,x}, n_{i,y})$ and $(t_{i,x}, t_{i,y})$ are the components of \mathbf{n}_i and \mathbf{t}_i , respectively; $[X_{i,0}, Y_{i,0}]^T$ and $[X_{i+1,0}, Y_{i+1,0}]^T$ are the initial position vectors of the nodes i and $i + 1$ at $t = 0$ in OXY , respectively; $[u_i, v_i, \varphi_i, u_{i+1}, v_{i+1}, \varphi_{i+1}]^T$ is the displacement vector of i and $i + 1$.

g_n^k can be calculated as follows:

$$g_n^k = [n_{i,x}, n_{i,y}, -n_{i,x}, -n_{i,y}] [X_k, Y_k, X_{k'}, Y_{k'}]^T \quad (6)$$

In terms of Eqs. (5) and (6), $\lambda_n^k \delta g_n^k$ can be easily determined as follows:

$$\begin{aligned} \lambda_n^k \delta g_n^k &= \delta[u_k, v_k, w_k, \theta_k, \phi_k, \varphi_k, u_i, v_i, \varphi_i, u_{i+1}, v_{i+1}, \varphi_{i+1}] \begin{bmatrix} n_{i,x} \cos \alpha_k + n_{i,y} \sin \alpha_k - n_{i,x} \sin \alpha_k \\ + n_{i,y} \cos \alpha_k, 0, 0, 0, 0, -n_{i,x} \beta_{k,1}^T - n_{i,y} \beta_{k,2}^T \end{bmatrix}^T \lambda_n^k \\ &= \delta[u_k, v_k, w_k, \theta_k, \phi_k, \varphi_k, u_i, v_i, \varphi_i, u_{i+1}, v_{i+1}, \varphi_{i+1}] \mathbf{B}_{c,n}^k \lambda_n^k \end{aligned} \quad (7)$$

(2) *Contact constrained matrix in the circumferential and the axial directions* The circumferential and the axial contact constrained matrices are determined via Hamilton's principle, as is shown in Eqs. (8) and (9).

$$\begin{cases} \lambda_t^k \delta g_t^k = \delta[u_k, v_k, w_k, \theta_k, \phi_k, \varphi_k, u_i, v_i, \varphi_i, u_{i+1}, v_{i+1}, \varphi_{i+1}] \mathbf{B}_{c,t}^k \lambda_n^k \\ \mathbf{B}_{c,t}^k = \mu \cos \vartheta_t^k [\boldsymbol{\eta}_k^T \boldsymbol{\gamma}_k^T]^T \\ \boldsymbol{\eta}_k = [t_{i,x} \cos \alpha_k + t_{i,y} \sin \alpha_k, -t_{i,x} \sin \alpha_k + t_{i,y} \cos \alpha_k, 0, 0, 0, 0]^T \\ \boldsymbol{\gamma}_k = -[t_{i,x} N_{u1}(\xi_k), t_{i,y} N_{u1}(\xi_k), 0, t_{i,x} N_{u2}(\xi_k), t_{i,y} N_{u2}(\xi_k), 0]^T \end{cases} \quad (8)$$

$$\begin{cases} \lambda_s^k \delta g_s^k = \delta[u_k, v_k, w_k, \theta_k, \phi_k, \varphi_k, u_i, v_i, \varphi_i, u_{i+1}, v_{i+1}, \varphi_{i+1}] \mathbf{B}_{c,s}^k \lambda_n^k \\ \mathbf{B}_{c,s}^k = \mu \cos \vartheta_s^k [0, 0, 1, 0]^T \end{cases} \quad (9)$$

where ϑ_t^k and ϑ_s^k are the angles between the total interface sliding friction and t_i -/ s_i - direction, respectively.

2.4. Model reduction

The equations of motion of the system with contact-impact can be written as follows:

$$\mathbf{M} \ddot{\mathbf{u}} + (\mathbf{C} + \mathbf{D}) \dot{\mathbf{u}} + \mathbf{K} \mathbf{u} + \mathbf{B}_c \lambda_N = \mathbf{F}_{\text{ext}} \quad (10)$$

where \mathbf{M} , \mathbf{C} , \mathbf{D} , and \mathbf{K} are the mass, Coriolis/gyroscopic, Rayleigh damping, and stiffness matrices, respectively; \mathbf{B}_c is the total contact constraint matrix; $\ddot{\mathbf{u}}$, $\dot{\mathbf{u}}$, and \mathbf{u} are the acceleration, velocity and displacement vectors, respectively; λ_N and \mathbf{F}_{ext} are the Lagrange multiplier and external force vectors, respectively. And

$$\mathbf{M} = \begin{bmatrix} \mathbf{M}_d & \mathbf{0} & \mathbf{0} & \mathbf{0} & \mathbf{0} \\ \mathbf{0} & \mathbf{M}_{b1} & \mathbf{0} & \mathbf{0} & \mathbf{0} \\ \mathbf{0} & \mathbf{0} & \ddots & \mathbf{0} & \mathbf{0} \\ \mathbf{0} & \mathbf{0} & \mathbf{0} & \mathbf{M}_{bN_b} & \mathbf{0} \\ \mathbf{0} & \mathbf{0} & \mathbf{0} & \mathbf{0} & \mathbf{M}_c \end{bmatrix}, \quad \mathbf{C} = \begin{bmatrix} \mathbf{C}_d & \mathbf{0} & \mathbf{0} & \mathbf{0} & \mathbf{0} \\ \mathbf{0} & \mathbf{C}_{b1} & \mathbf{0} & \mathbf{0} & \mathbf{0} \\ \mathbf{0} & \mathbf{0} & \ddots & \mathbf{0} & \mathbf{0} \\ \mathbf{0} & \mathbf{0} & \mathbf{0} & \mathbf{C}_{bN_b} & \mathbf{0} \\ \mathbf{0} & \mathbf{0} & \mathbf{0} & \mathbf{0} & \mathbf{0} \end{bmatrix}, \quad \mathbf{D} = \begin{bmatrix} \alpha_{bd} \mathbf{M}_{bd} + \beta_{bd} \mathbf{K}_{bd} & \mathbf{0} \\ \mathbf{0} & \alpha_c \mathbf{M}_c + \beta_c \mathbf{K}_c^e \end{bmatrix} \quad (11a)$$

$$\begin{aligned} \mathbf{B}_c &= [\mathbf{B}_{c,n}^1 + \mathbf{B}_{c,t}^1 + \mathbf{B}_{c,s}^1 \quad \cdots \quad \mathbf{B}_{c,n}^{N_{cp}} + \mathbf{B}_{c,t}^{N_{cp}} + \mathbf{B}_{c,s}^{N_{cp}}], \quad \mathbf{u} = [\mathbf{u}_d^T, \mathbf{u}_b^T, \mathbf{u}_c^T]^T, \quad \lambda_N = [\lambda_N^1 \quad \cdots \quad \lambda_N^{N_{cp}}], \\ \mathbf{F}_{\text{ext}} &= [(\mathbf{F}_{\text{ext}}^d), (\mathbf{F}_{\text{ext}}^b), \mathbf{0}]^T \end{aligned} \quad (11b)$$

$$\mathbf{K} = \begin{bmatrix} \begin{bmatrix} \mathbf{K}_d^c + \mathbf{K}_{\text{rigid}} \\ + (\sum_{i=1}^{N_b} \mathbf{K}_{db}^i)_d \end{bmatrix} & (\mathbf{K}_{db}^1)_{db} & \cdots & (\mathbf{K}_{db}^{N_b})_{db} & \mathbf{0} \\ (\mathbf{K}_{db}^1)_{db} & \begin{bmatrix} \mathbf{K}_{b1}^e + \mathbf{K}_{b1}^c \\ + \mathbf{K}_{b1}^s + (\mathbf{K}_{db}^1)_b \end{bmatrix} & \mathbf{0} & \mathbf{0} & \mathbf{0} \\ \vdots & \mathbf{0} & \ddots & \mathbf{0} & \mathbf{0} \\ (\mathbf{K}_{db}^{N_b})_{db} & \mathbf{0} & \mathbf{0} & \begin{bmatrix} \mathbf{K}_{bN_b}^e + \mathbf{K}_{bN_b}^c \\ + \mathbf{K}_{bN_b}^s + (\mathbf{K}_{db}^{N_b})_b \end{bmatrix} & \mathbf{0} \\ \mathbf{0} & \mathbf{0} & \mathbf{0} & \mathbf{0} & \mathbf{K}_c^e \end{bmatrix} \quad (11c)$$

where N_{cp} represents the number of the blade contacting with the casing.

Considering a high number of degrees of freedom (DoFs) of the blisk-casing system with elastic supports, the model reduction is essential to improve computational efficiency [64]. In this paper, the Craig-Bampton method (CBM) in Refs. [38,59] is applied to build corresponding reduced models. By definition, the DoFs of the component such as the disk, the blade or the casing should be firstly separated into the slave and master DoFs. Corresponding equations of motion are then written as follows:

$$\begin{bmatrix} \mathbf{M}_{ss}^X & \mathbf{M}_{sm}^X \\ \mathbf{M}_{ms}^X & \mathbf{M}_{mm}^X \end{bmatrix} \begin{bmatrix} \dot{\mathbf{u}}_s^X \\ \dot{\mathbf{u}}_m^X \end{bmatrix} + \begin{bmatrix} \mathbf{C}_{ss}^X & \mathbf{C}_{sm}^X \\ \mathbf{C}_{ms}^X & \mathbf{C}_{mm}^X \end{bmatrix} \begin{bmatrix} \dot{\mathbf{u}}_s^X \\ \dot{\mathbf{u}}_m^X \end{bmatrix} + \begin{bmatrix} \mathbf{K}_{ss}^X & \mathbf{K}_{sm}^X \\ \mathbf{K}_{ms}^X & \mathbf{K}_{mm}^X \end{bmatrix} \begin{bmatrix} \mathbf{u}_s^X \\ \mathbf{u}_m^X \end{bmatrix} = \begin{bmatrix} \mathbf{F}_s^{X,\text{ext}} \\ \mathbf{F}_m^{X,\text{ext}} \end{bmatrix} \quad (12)$$

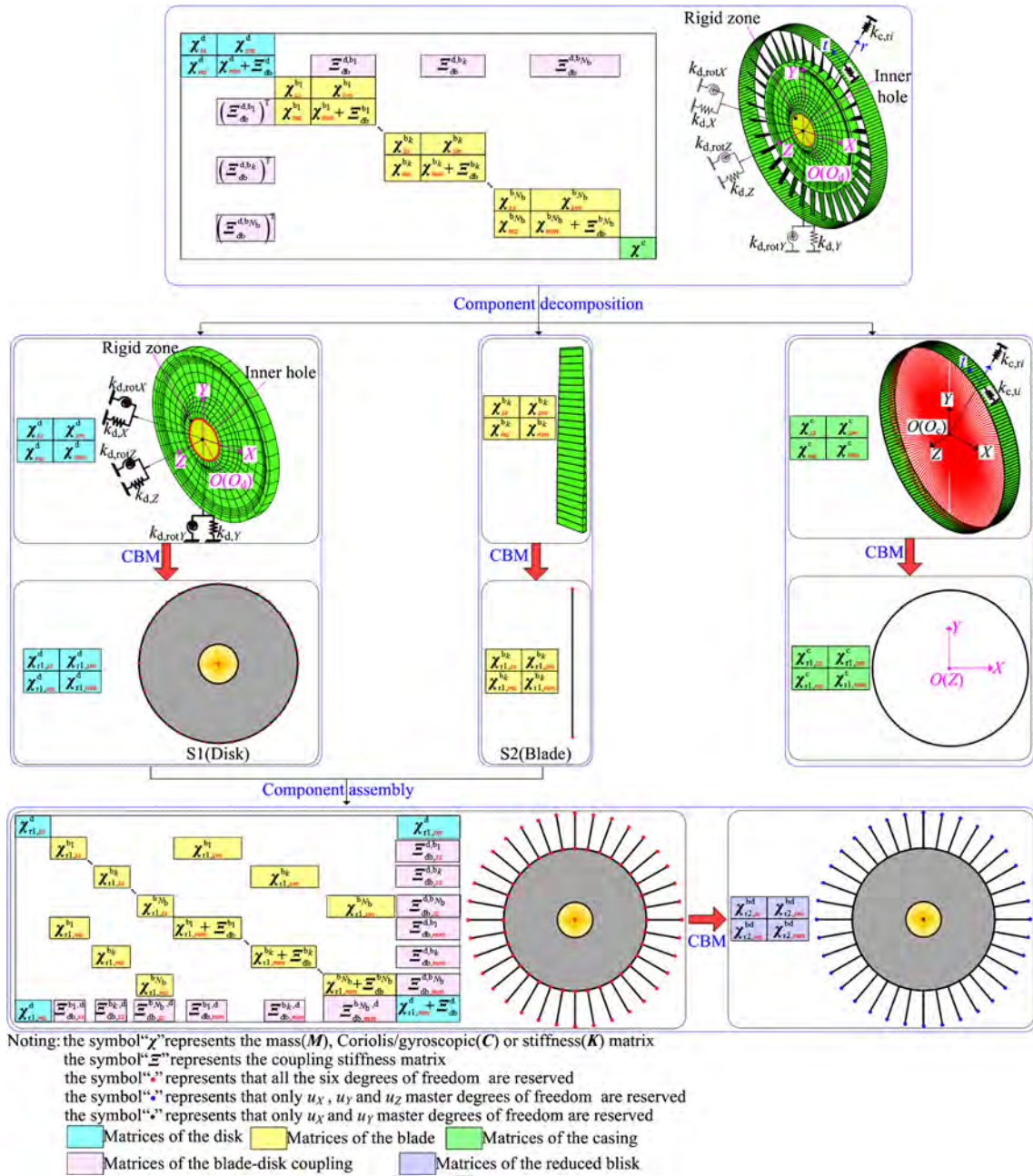


Fig. 5. Flow chart of the reduced blisk-casing system.

where the superscript X represents the disk, blade or the casing component; M , C , and K are the mass, Coriolis/gyroscopic and stiffness matrices, respectively; F is the external force vector; the subscripts 's' and 'm' represent the slave and master DoFs, respectively; u , \dot{u} and \ddot{u} are the displacement, velocity and acceleration vectors, respectively.

In terms of CBM (see Refs. [38,59]), the relationship between the physical DoFs u^X and the generalized DoFs q^X can be expressed as follows:

$$u^X = \begin{bmatrix} u_s^X \\ u_m^X \end{bmatrix} = \begin{bmatrix} (\Phi_{ss}^X)_l & \Phi_{sm}^X \\ 0 & I_{mm}^X \end{bmatrix} \begin{bmatrix} q_s^X \\ q_m^X \end{bmatrix} = \Phi^X q^X \quad (13)$$

where $\Phi_{sm}^X = -(\mathbf{K}_{ss}^X)^{-1} \mathbf{K}_{sm}^X$; $(\Phi_{ss}^X)_l$ is the reserved first- l order fixed interface normal modes.

Substituting Eq. (13) into Eq. (12), the equations of motion of the reduced component X can be written as follows:

$$\hat{M}^X \ddot{q}^X + \hat{C}^X \dot{q}^X + \hat{K}^X q^X = \hat{F}_{ext}^X \quad (14)$$

where $\hat{\chi}^X = (\Phi^X)^T \begin{bmatrix} \chi_{ss}^X & \chi_{sm}^X \\ \chi_{ms}^X & \chi_{mm}^X \end{bmatrix} \Phi^X$ ($\chi = M, C, K$).

In order to establish the final reduced blisk-casing system, the two-step reduction for the blisk and the one-step reduction for the casing are adopted, respectively. More detailed information on the model reduction is shown in Fig. 5. After the final reduction, the

Table 1
Material and geometrical parameter settings.

Component	Material parameters			Geometrical parameters (mm)	Supporting stiffness
	Density ρ (kg·m ⁻³)	Young's modulus E (GPa)	Poisson's ratio ν		
Disk [65]	8228.3	216.8	0.28	$b_1 = 23.9, b_2 = 42.5, b_3 = 116, b_4 = 46.5;$ $d_1 = 166.4, d_2 = 216, d_3 = 344, d_4 = 564,$ $d_5 = 626, d_6 = 664; ecc = 3 \times 10^{-4}$	$k_{d,X} = k_{d,Y} = 1 \times 10^8$ N/m, $k_{d,Z} = 1 \times 10^9$ N/m, $k_{d,rot X} = k_{d,rot Y} = 6 \times 10^5$ N/m, $k_{d,rot Z} = 1 \times 10^7$ N/m
Blade				$L = 160, b_0 = 25.2, h_0 = 4.2, \beta_0 = 15^\circ,$ $\gamma(L) = 45^\circ, \kappa = 5/6, \tau_b = 0.3056, \tau_h = 0.4048$	–
Casing	4430	113	0.33	$R_{c,min} = 493.5, R_{c,max} = 503.5,$ $h_c = 2, b_c = 100, \kappa = 5/6$	$k_{c,r} = k_{c,t} = 2 \times 10^4$ N/m

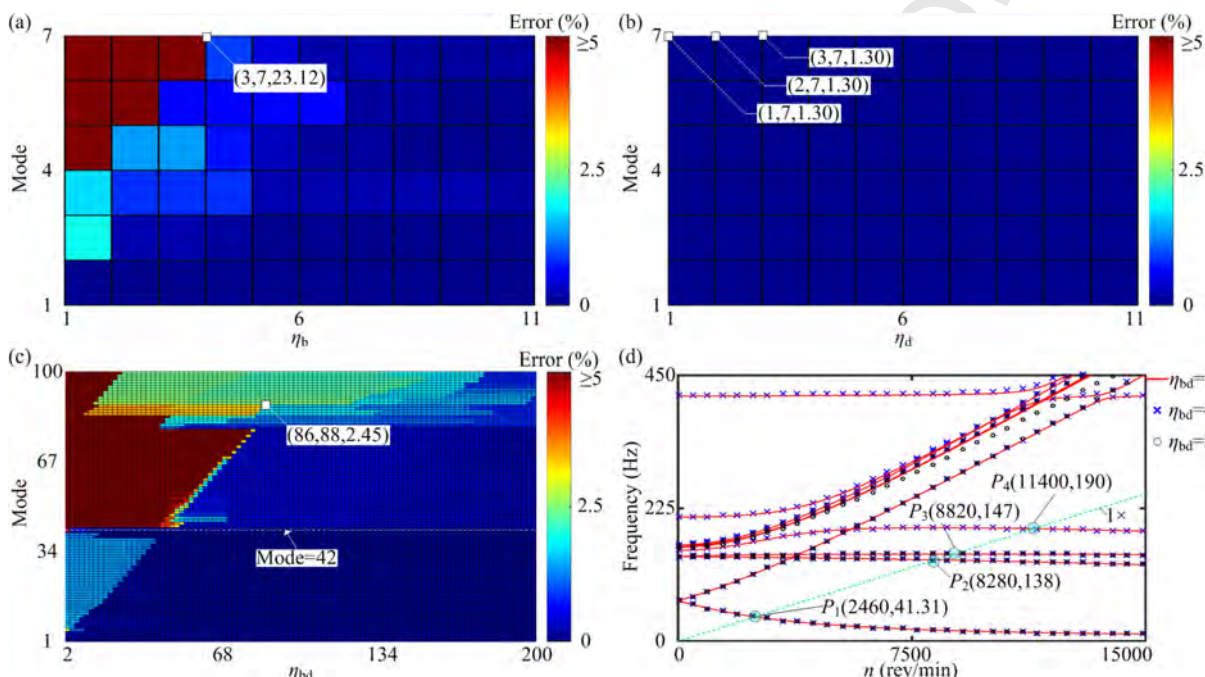


Fig. 6. Effects of mode truncation numbers η_b , η_d and η_{bd} : (a) single blade, (b) single disk, (c) blisk, (d) Campbell diagram of the blisk.

equations of motion of the reduced system with Rayleigh damping and contact-impact considered can be rewritten as follows:

$$\hat{M}\ddot{\mathbf{q}} + (\hat{C} + \hat{D})\dot{\mathbf{q}} + \hat{K}\mathbf{q} + \hat{B}_c\lambda_N = \hat{\mathbf{F}}_{\text{ext}} \quad (15)$$

3. Numerical examples

3.1. Model reduction of the blisk-casing coupled system

A numerical case is exemplified here to verify the model reduction techniques proposed in Subsection 2.4. Corresponding parameter settings of the disk, the blade, and the casing are listed in Table 1. In light of the final reduced blisk model originated from the two-step Craig-Bampton reduction (see Fig. 5), the effect of each reduction on the model accuracy should be verified firstly. In this paper, the natural frequency of the blisk is an indicator to obtain the appropriate mode truncation number.

The first-seven order frequency convergence of the single blade and the single disk under $n = 0$ rev/min is shown in Figs. 6(a) and 6(b), respectively, while the first-one hundred order frequency convergence of the blisk under $n = 0$ rev/min is shown in Fig. 6(c). Here, it should be noted that all the frequency errors in Figs. 6(a)–6(c) is calculated via the comparisons between the reduced model and the full model (benchmark). It can be concluded from Figs. 6(a)–6(c) that the smaller the mode truncation number is, the larger the frequency error close to higher-order frequency is. Here, the mode truncation numbers $\eta_b = 4$ for the single blade and $\eta_d = 4$ for the single disk are sufficient to accurately calculate corresponding first-seven order natural frequencies when performing the first Craig-Bampton reduction (see Figs. 5, 6(a), and 6(b)), and the mode truncation number $\eta_{bd} = 86$ for the blisk is sufficient to accurately calculate the first-one hundred order natural frequencies of the blisk when performing the second Craig-Bampton reduction (see Figs. 5 and 6(c)). Considering the effect of the unbalance load with the excitation frequency $1 \times n/60$ located at the disk center O_d , the variation of the dynamic frequencies of the blisk is plotted in Fig. 6(d) when the rotating speed $n \in [0, 15000]$ rev/min, and the results obtained from $\eta_{bd} = 86$ are as a benchmark. It can be seen from Fig. 6(d) that $\eta_{bd} = 4$ are sufficient to simulate the dynamic characteristics of the blisk for the studied operating conditions.

In this paper, $\eta_b = \eta_d = 4$ is adopted to establish the final reduced blisk model. Here, it should be noted that $\eta_{bd} = 4$ can only guarantee the accuracy of the first-forty-two order natural frequencies (see Fig. 6(c)). In order to identify the dominated modes of

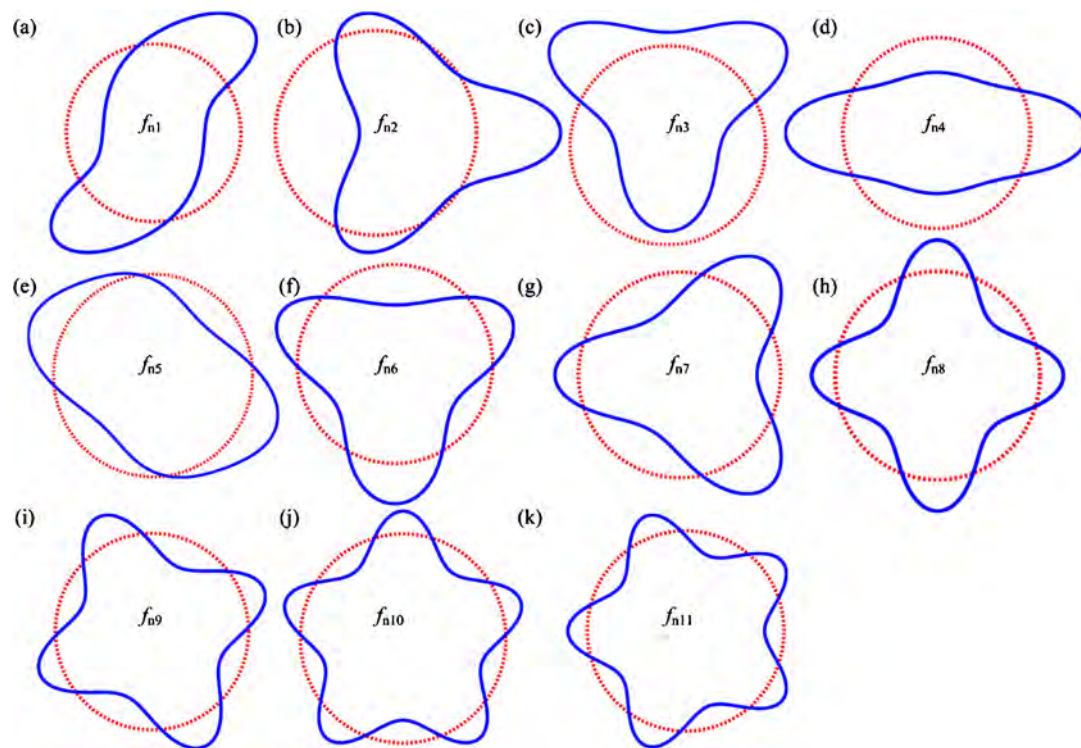
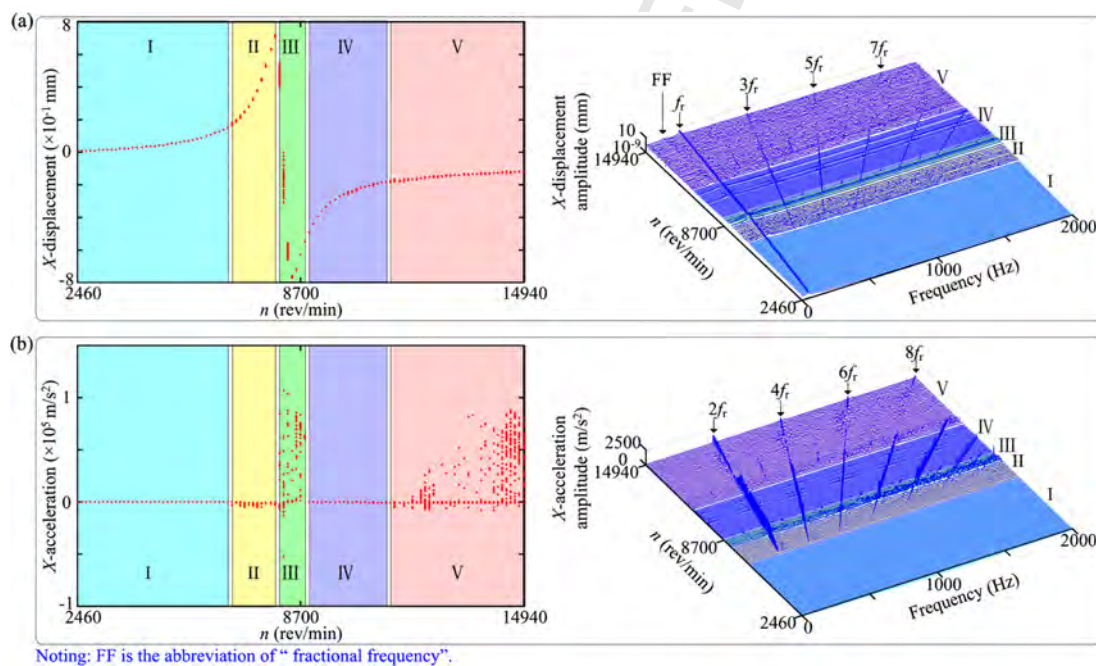


Fig. 9. First-eleven order modes of the casing: (a) 180.98 Hz, (b) 181.04 Hz, (c) 181.05 Hz, (d) 181.22 Hz, (e) 181.54 Hz, (f) 181.99 Hz, (g) 181.99 Hz, (h) 183.35 Hz, (i) 183.36 Hz, (j) 186.54 Hz, (k) 186.54 Hz.



Noting: FF is the abbreviation of "fractional frequency".

Fig. 10. Bifurcation diagram and spectrum cascade in X-direction: (a) the blisk, (b) the casing.

P_1 at the last moment (see Fig. 11) is regarded as the reference point, and the points such as P_2, P_3, \dots , and P_{49} are then extracted in sequence every $1/f_r$ s. Similarly, the bifurcation points at other rotating speeds can be also obtained. Next, taking n as abscissa and bifurcation points as ordinate, the bifurcation diagram of the blisk in X-direction can be then obtained, as is shown in Fig. 10(a). The bifurcation diagram of the casing (see the left column in Fig. 10(b)) can be drawn in a similar way and no more tautology here.

In order to show the distribution rules in the rubbing regions II, III, IV, and V clearly, corresponding enlarged views are supplemented in Figs. 12–15. In these figures, Δn is further set as 30 rev/min. Some main phenomena are concluded as follows:

(1) With the increasing n , the motion of the blisks successively experiences period-1 motion (see the regions I and II in Figs. 10(a) and 12(a)) \rightarrow chaotic motion to period-1 motion (see the region III in the left column in Fig. 13) \rightarrow switch between period-1 and chaotic motions (see the region IV in Fig. 14(a)) \rightarrow chaotic motion (see the region V in Fig. 15(a)), while the motion of the casing successively

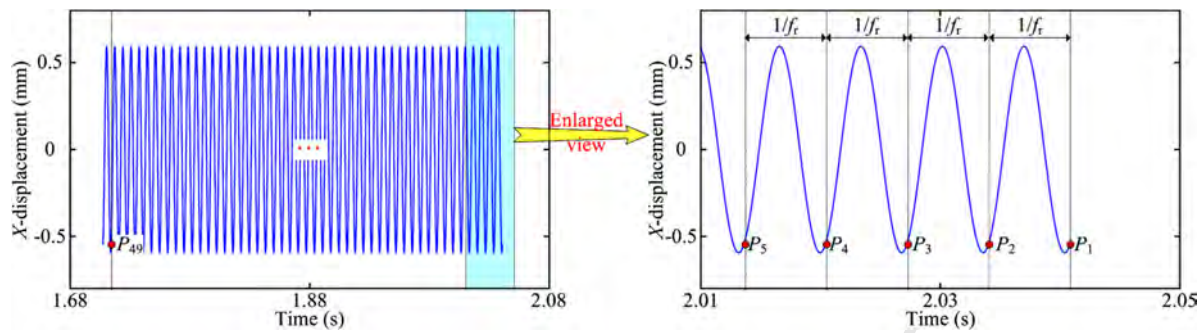


Fig. 11. X-displacement time-domain waveforms of the blisk in the last $49/f_r$ s.

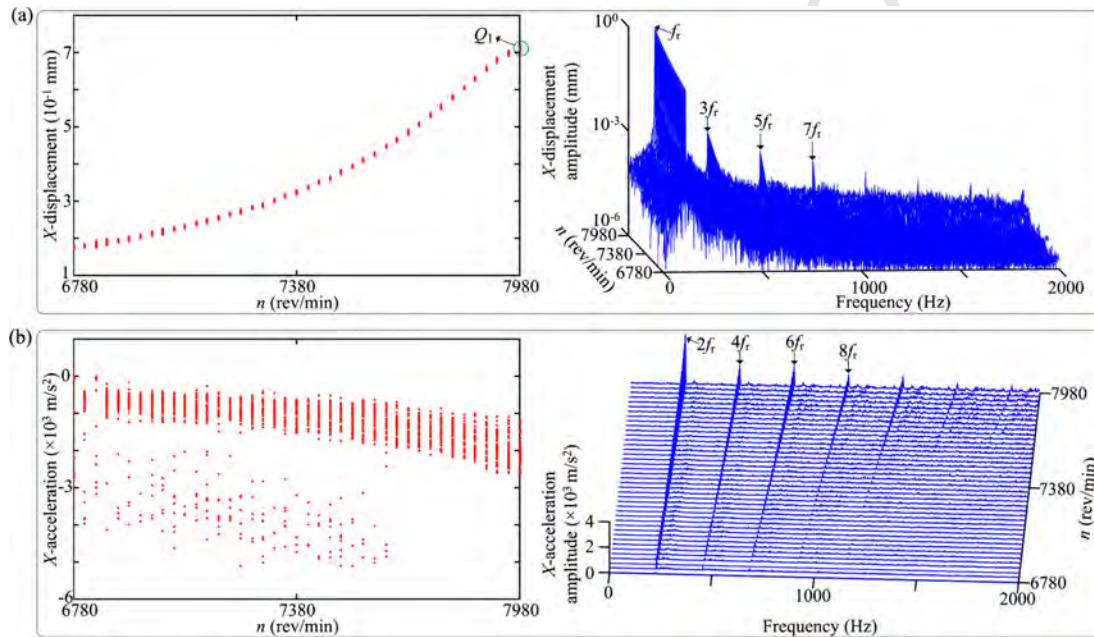


Fig. 12. Enlarged view of the region II: (a) the blisk, (b) the casing.

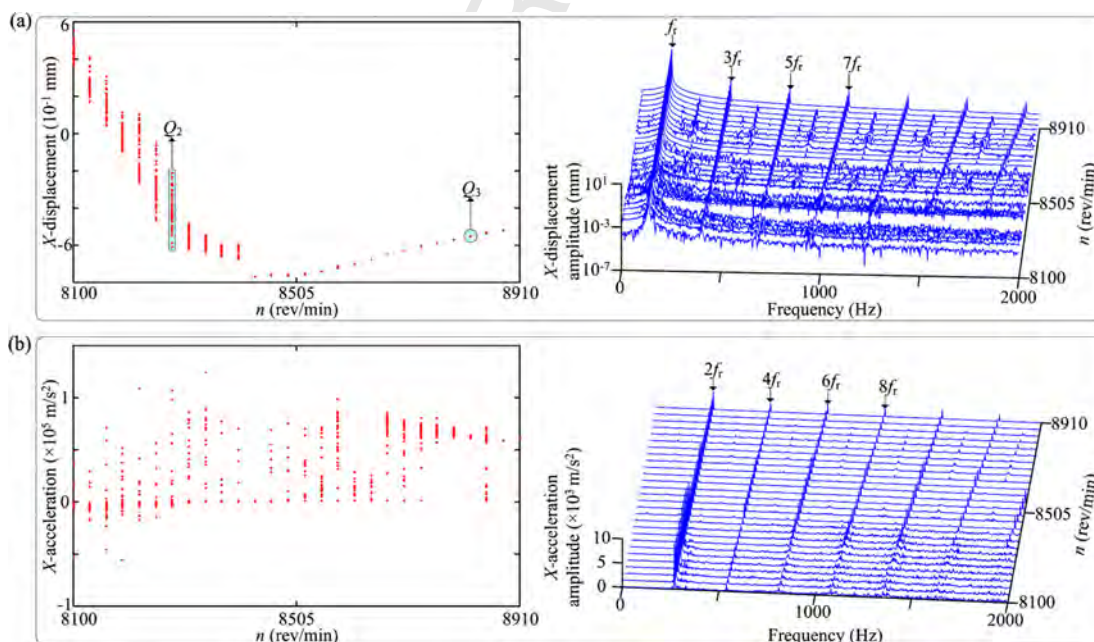


Fig. 13. Enlarged view of the region III: (a) the blisk, (b) the casing.

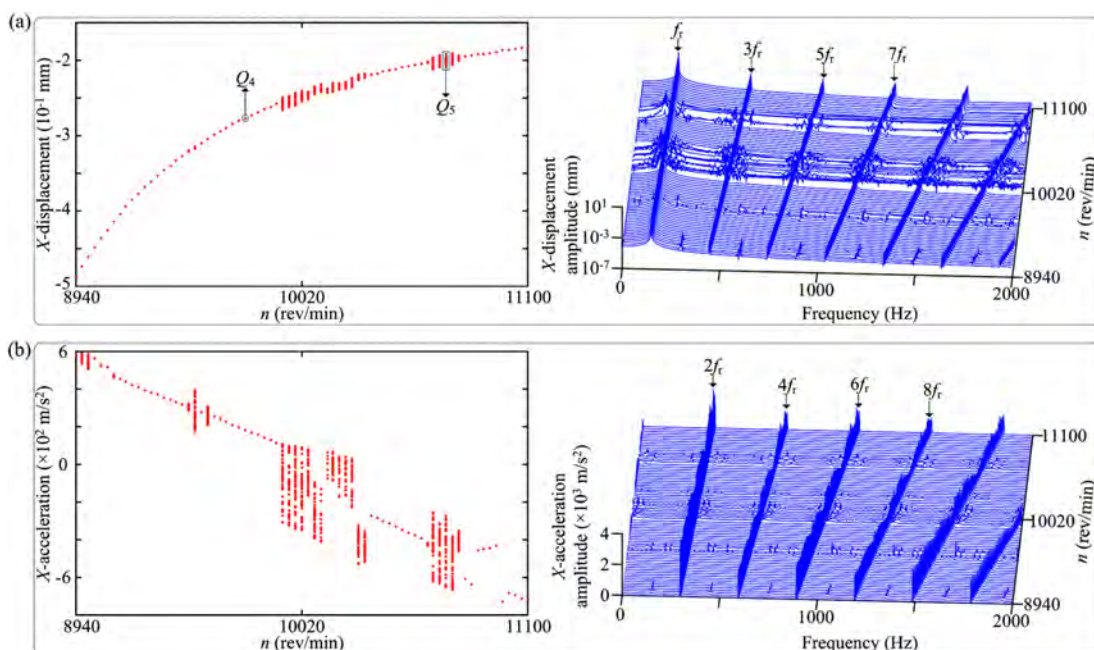
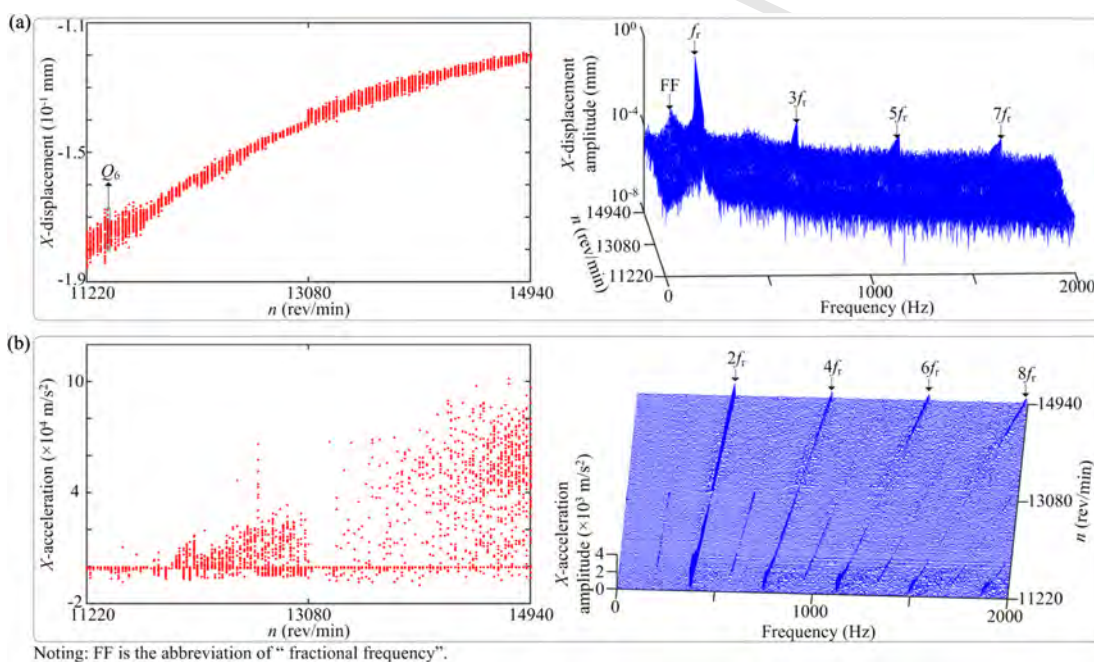


Fig. 14. Enlarged view of the region IV: (a) the blisk, (b) the casing.



Noting: FF is the abbreviation of "fractional frequency".

Fig. 15. Enlarged view of the region V: (a) the blisk, (b) the casing.

experiences static state (see the region I in Fig. 10(b)) → chaotic motion (see the region II in Fig. 12(b)) → switch among chaotic, multi-period, and period-1 motions (see the region III in Fig. 13(b)) → switch between chaotic and period-1 motions (see the region IV in Fig. 14(b)) → chaotic motion (see the region V in Fig. 15(b)). Here, it should be pointed out that in terms of the region I in Fig. 10, due to the non-existence of the rubbing between the blades and the casing, only the period-1 motion and f_r for the blisk can be observed (see Fig. 10(a)), while only static state for the casing is existent (see Fig. 10(b)). In addition, the reason for the point-set scattering in the regions III and V is that the former region is close to the critical speed of the system (see Fig. 6(d)) and the latter region is located at the high-speed zone, which can aggravate the degree of rubbing.

(2) In terms of the spectrum cascade shown in Figs. 10, 12–15, the significant phenomenon is that the odd-harmonic frequencies ($f_r, 3f_r, 5f_r, \dots$) for the blisk and the even-harmonic frequencies ($2f_r, 4f_r, 6f_r, \dots$) for the casing are prominent. Especially when n is larger, the fractional frequency (FF) occurs (see the region V in Figs. 10 and 15).

In order to further understand the dynamic characteristics of the system located at the rubbing regions II, III, IV and V, the distribution characteristics of the contact zone on the casing and the blades at local speeds $n = 7980$ rev/min (see Q_1 in Fig. 12), 8280 rev/min (see Q_2 in Fig. 13), 8820 rev/min (see Q_3 in Fig. 13), 9750 rev/min (see Q_4 in Fig. 14), 10710 rev/min (see Q_5 in Fig. 14), and 11400 rev/min (see Q_6 in Fig. 15) are then extracted, respectively, as is shown in Fig. 16. Obviously, due to the oval configuration of the casing (see

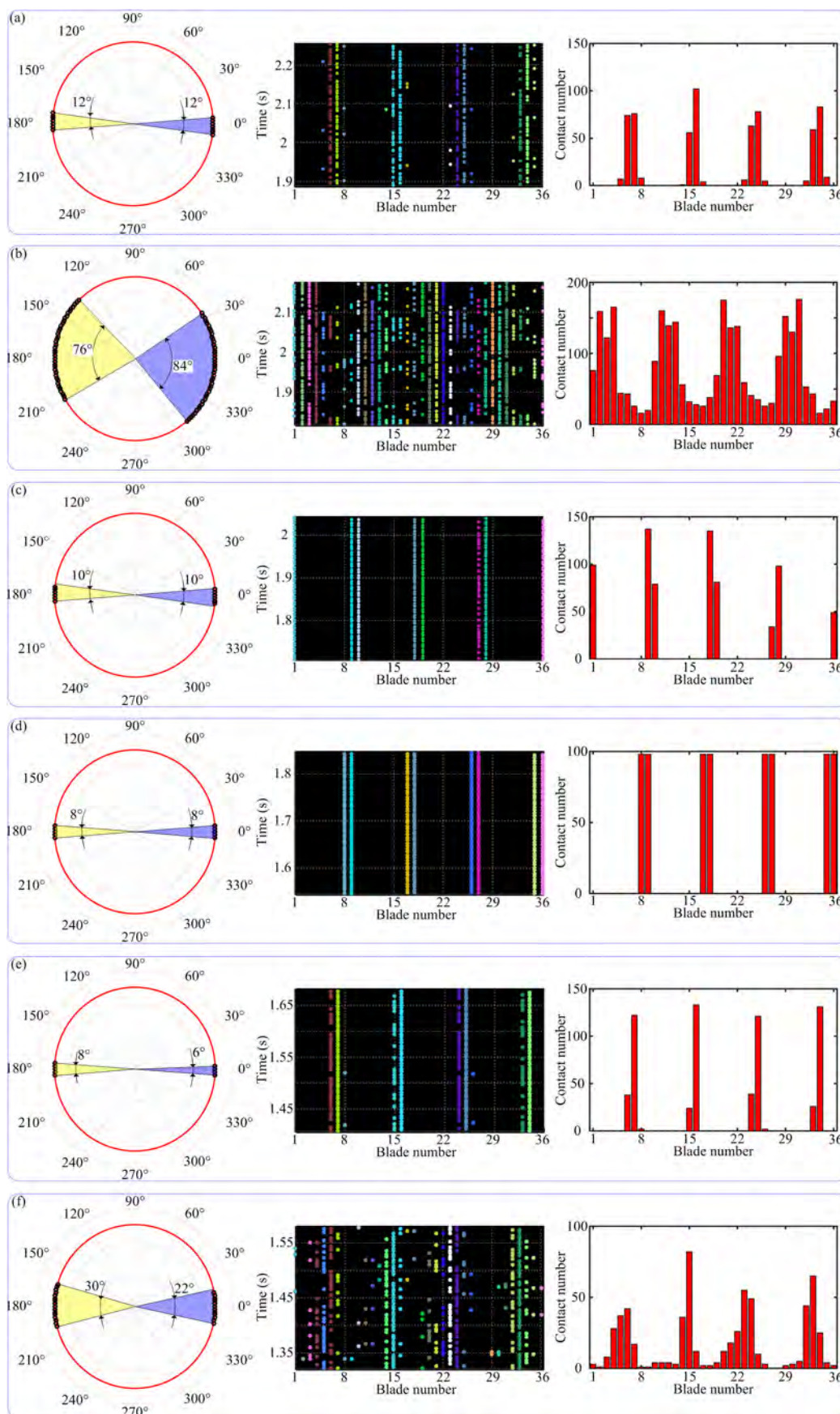


Fig. 16. Distribution of the rubbing positions on the casing and the blades in the last $49/f_r$ s: (a) 7980 rev/min, (b) 8280 rev/min, (c) 8820 rev/min, (d) 9750 rev/min, (e) 10710 rev/min, (f) 11400 rev/min.

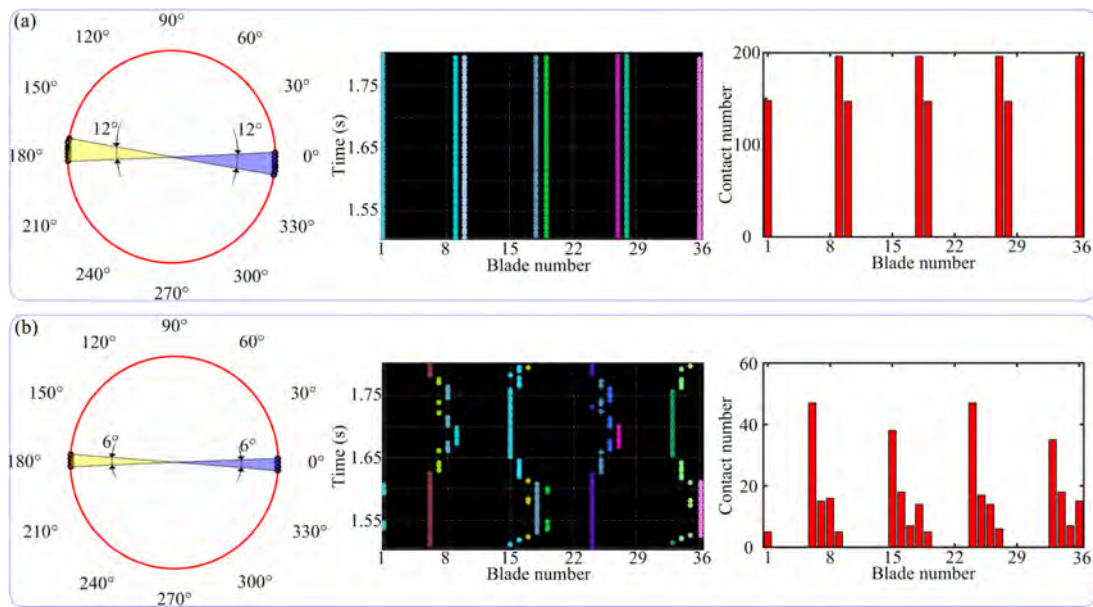


Fig. 18. Distribution of the rubbing positions on the casing and the blades in the last $49/f_r$ s: (a) $k_{d,x}/k_{d,y} = 1.4 \times 10^8$ N/m, (b) $k_{d,x}/k_{d,y} = 4.55 \times 10^8$ N/m.

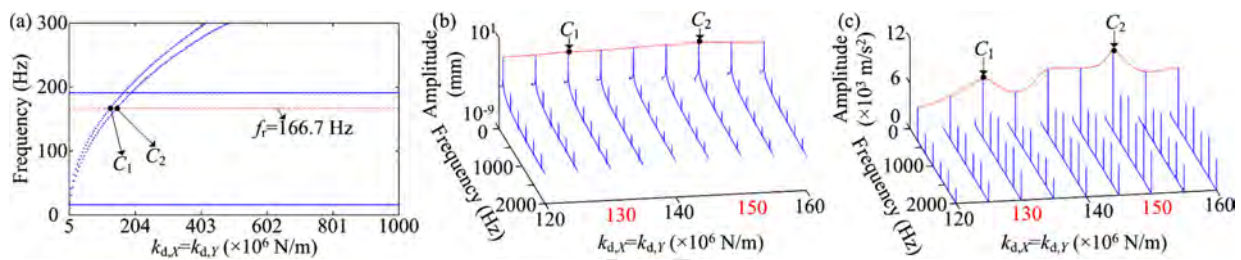


Fig. 19. Effects of $k_{d,x}/k_{d,y}$ on the natural frequencies of the blisk: (a) frequency curve, (b) region I in the spectrum of the blisk in Fig. 17, (c) region I in the spectrum of the casing in Fig. 17.

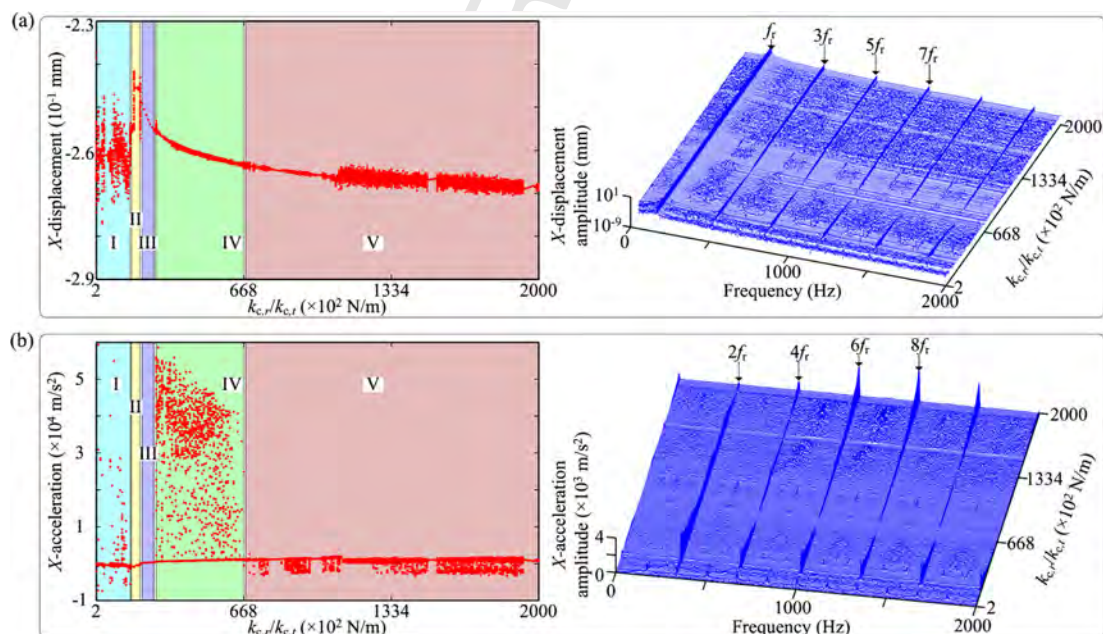


Fig. 20. Bifurcation diagram and spectrum cascade in X-direction: (a) the blisk, (b) the casing.

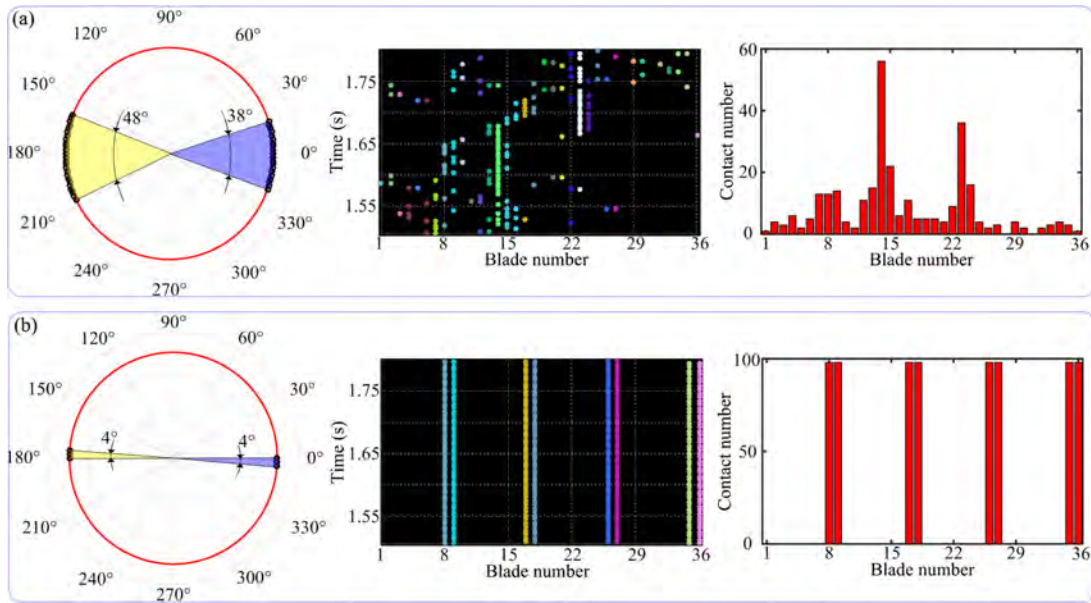


Fig. 21. Distribution of the rubbing positions on the casing and the blades in the last 49/ f_r s: (a) $k_{c,r}/k_{c,t} = 3.8 \times 10^3$ N/m, (b) $k_{c,r}/k_{c,t} = 2.27 \times 10^4$ N/m.

3.3.2. Effects of supporting stiffness of the casing

Relative to the effects of $k_{d,X}/k_{d,Y}$ on the rubbing dynamics of the system shown in Subsection 3.3.1, $k_{c,r}/k_{c,t}$ has more significant effects on the rubbing characteristics of the system, as is shown in Fig. 20. These figures show the following dynamic phenomena:

(1) In terms of the bliks, period-1 motion is observed only in the region III ($k_{c,r}/k_{c,t} \in [209, 263] \times 10^6$ N/m), and the chaotic motion in the regions I ($k_{c,r}/k_{c,t} \in [2, 155] \times 10^6$ N/m), II ($k_{c,r}/k_{c,t} \in [164, 200] \times 10^6$ N/m), IV ($k_{c,r}/k_{c,t} \in [272, 668] \times 10^6$ N/m), and V ($k_{c,r}/k_{c,t} \in [677, 2000] \times 10^6$ N/m) widely exists (see the left column in Fig. 20(a)); in terms of the casing, period-1 motion exists in the regions II and III, and chaotic motion mostly exists in other regions (see the left column in Fig. 20(b)).

(2) The spectrum cascade shows that the odd-harmonic frequencies ($f_r, 3f_r, 5f_r, \dots$) for the blisk and the even-harmonic frequencies ($2f_r, 4f_r, 6f_r, \dots$) for the casing are prominent (see the right column in Fig. 20), which also corresponds to that in Figs. 10 and 17.

The distributions of the rubbing positions on the casing and the blades at local $k_{c,r}/k_{c,t}$ are shown in Fig. 21. Generally speaking, the smaller $k_{c,r}/k_{c,t}$ is, the larger the contact area is (see the left column in Fig. 21). In addition, period-1 motion/chaotic motion for the blisk corresponds to the equal/unequal and radially symmetric contact zones on the casing (see the left column in Fig. 21), which can be also verified by Figs. 16 and 18.

4. Conclusions

In this paper, the finite element model of the blisk-oval casing system with elastic supports is established using the self-programmed beam-shell-spring hybrid elements combining with two types of self-programmed interfacial coupling elements (ICEs). In order to improve computational efficiency, the two-step reduction for the blisk and the one-step reduction for the casing are adopted to establish the reduced blisk-casing system. Then the reduced system is verified via the frequency convergence analysis. Next, the central difference method combining with the Lagrange multiplier method is adopted to solve the rubbing dynamic characteristics of the system under different rotating speeds and supporting stiffness. Some main conclusions are summarized as follows:

(1) Under the premise of guaranteeing the accuracy and the computational efficiency of the system, only a few modes in the modal reduction basis are essential when using the Craig-Bampton method.

(2) The fundamental frequency in the spectrum of the casing is dependent on the rotating frequency of blisk and the number of contact zone on the casing. In addition, period-1 motion/chaotic motion for the blisk indicates the equal/unequal and radially symmetric contact zones on the casing, respectively.

(3) The change of the supporting stiffness on the casing has more significant effects on the dynamic characteristics of the system than that on the blisk. Besides, the vibration responses of the casing are more sensitive to the system state variations such as the occurrence of the resonance than those of the blisk.

Declaration of competing interest

The author(s) declared no potential conflicts of interest with respect to the research, authorship, and/or publication of this article.

Acknowledgement

This project is supported by the National Natural Science Foundation of China (Grant Nos. 11772089, 11972112), the Fundamental Research Funds for the Central Universities (Grant Nos. N170306004, N170308028, N180708009 and N180306005), Program for the Innovative Talents of Higher Learning Institutions of Liaoning (LR2017035), and LiaoNing Revitalization Talents Program (Grant No. XLYC1807008) for providing financial support for this work.

References

- [1] J. Slater, G.R. Minkiewicz, A.J. Blair, Forced response of bladed disk assemblies – a survey, *Shock Vib. Dig.* 31 (1) (1999) 17–24.
- [2] P. Höhnisch, A. Kühhorn, B. Beirrow, Experimental and numerical analyses of radial turbine blisks with regard to mistuning, in: *ASME Turbo Expo 2011: Turbine Technical Conference and Exposition*, 2011 June 6–10, Vancouver, British Columbia, Canada, ASME, New York, 2011, pp. 1–10.
- [3] F. Gao, W. Sun, J.N. Gao, Forced vibration analysis of the hard-coating blisk considering the strain-dependent manner of the hard-coating damper, *Aerosp. Sci. Technol.* 79 (2018) 187–198.
- [4] Y.G. Chen, J.Y. Zhai, Q.K. Han, Vibration and damping analysis of the bladed disk with damping hard coating on blades, *Aerosp. Sci. Technol.* 58 (2016) 248–257.
- [5] Y.G. Chen, H.C. Wu, J.Y. Zhai, H. Chen, Q.Y. Zhu, Q.K. Han, Vibration reduction of the blisk by damping hard coating and its intentional mistuning design, *Aerosp. Sci. Technol.* 84 (2019) 1049–1058.
- [6] Z. Luo, Y. Wang, J.Y. Zhai, Y.P. Zhu, D.Y. Wang, Prediction of vibration characteristics of blisks using similitude models, *Mech. Based Des. Struct. Mach.* 47 (2) (2019) 121–135.
- [7] C.M. Mehalić, J.A. Ziemianski, Performance deterioration of commercial high-bypass ratio turbofan engines, in: *The SAE Aerospace Congress*, 1980 October 13–16, Los Angeles, California, USA, NASA, Washington, 1980, pp. 1–30.
- [8] H. Ma, F.L. Yin, Y.Z. Guo, X.Y. Tai, B.C. Wen, A review on dynamic characteristics of blade-casing rubbing, *Nonlinear Dyn.* 84 (2016) 437–472.
- [9] Y.M. Liu, M.W. Zhao, C.Z. Sun, M. Hu, D.Y. Chen, Z.W. Liu, J.B. Tan, A method to minimize stage-by-stage initial unbalance in the aero engine assembly of multistage rotors, *Aerosp. Sci. Technol.* 85 (2019) 270–276.
- [10] E.P. Petrov, Reduction of forced response levels for bladed disks by mistuning: overview of the phenomenon, *J. Eng. Gas Turbines Power* 133 (7) (2011) 1–10.
- [11] I. Lee, S.J. Shin, Y.R. Kim, Mistuned bladed disk forced vibration analysis based on standing wave formulation, *Aerosp. Sci. Technol.* 24 (1) (2013) 275–282.
- [12] R. Corral, O. Khemiri, C. Martel, Design of mistuning patterns to control the vibration amplitude of unstable rotor blades, *Aerosp. Sci. Technol.* 80 (2018) 20–28.
- [13] B. Bai, G.C. Bai, C. Li, Application of multi-stage multi-objective multi-disciplinary agent model based on dynamic substructural method in Mistuned Blisk, *Aerosp. Sci. Technol.* 46 (2015) 104–115.
- [14] A. Muszynska, Rotor-to-stationary element rubbing-related vibration phenomena in rotating machinery-Literature survey, *Shock Vib. Dig.* 21 (3) (1989) 3–11.
- [15] H.J. Xuan, R.R. Wu, Aeroengine turbine blade containment tests using high-speed rotor spin testing facility, *Aerosp. Sci. Technol.* 10 (6) (2006) 501–508.
- [16] M. Legrand, C. Pierre, P. Cartraud, J.P. Lombard, Two-dimensional modeling of an aircraft engine structural bladed disk-casing modal interaction, *J. Sound Vib.* 319 (1–2) (2009) 366–391.
- [17] H. Ma, Y. Lu, Z.Y. Wu, X.Y. Tai, B.C. Wen, Vibration response analysis of a rotational shaft-disk-blade system with blade-tip rubbing, *Int. J. Mech. Sci.* 107 (2016) 110–125.
- [18] H. Ma, X.Y. Tai, Q.K. Han, Z.Y. Wu, D. Wang, B.C. Wen, A revised model for rubbing between rotating blade and elastic casing, *J. Sound Vib.* 337 (2015) 301–320.
- [19] H. Ma, F.L. Yin, X.Y. Tai, D. Wang, B.C. Wen, Vibration response analysis caused by rubbing between rotating blade and casing, *J. Mech. Sci. Technol.* 30 (5) (2016) 1983–1995.
- [20] N. Lesaffre, J.J. Sinou, F. Thouverez, Stability analysis of rotating beams rubbing on an elastic circular structure, *J. Sound Vib.* 299 (4–5) (2007) 1005–1032.
- [21] B.Q. Li, H. Ma, J. Zeng, X.M. Guo, B.C. Wen, Rotating blade-casing rubbing simulation considering casing flexibility, *Int. J. Mech. Sci.* 148 (2018) 118–134.
- [22] H.J. Kou, J.J. Du, M.X. Liang, L. Zhu, L. Zeng, Z.D. Zhu, F. Zhang, Nonlinear characteristics of contact-induced vibrations of the rotating variable thickness plate under large deformations, *Eur. J. Mech. A, Solids* (2019) 1–29, <https://doi.org/10.1016/j.euromechsol.2019.103801>.
- [23] H.J. Kou, H.Q. Yuan, Rub-induced non-linear vibrations of a rotating large deflection plate, *Int. J. Non-Linear Mech.* 58 (2014) 283–294.
- [24] Q. Sun, H. Ma, Y.P. Zhu, Q.K. Han, B.C. Wen, Comparison of rubbing induced vibration responses using varying-thickness-twisted shell and solid-element blade models, *Mech. Syst. Signal Process.* 108 (2018) 1–20.
- [25] M. Legrand, A. Batailly, B. Magnain, P. Cartraud, C. Pierre, Full three-dimensional investigation of structural contact interactions in turbomachines, *J. Sound Vib.* 331 (11) (2012) 2578–2601.
- [26] Z.K. He, H.J. Xuan, C.E. Bai, Y.Q. Hu, P.H. Cong, H.S. Bai, Y. Miao, W.R. Hong, Containment tests and analysis of soft wall casing fabricated by wrapping Kevlar fabric around thin metal ring, *Aerosp. Sci. Technol.* 61 (2017) 35–44.
- [27] A. Batailly, M. Legrand, A. Millecamps, F. Garcin, Numerical-experimental comparison in the simulation of rotor/stator interaction through blade-tip/abradable coating contact, *J. Eng. Gas Turbines Power* 134 (8) (2012) 1–11.
- [28] A. Batailly, M. Legrand, C. Pierre, Full three-dimensional rotor/stator interaction simulations in aircraft engines with time-dependent angular speed, *J. Eng. Gas Turbines Power* 139 (3) (2017) 1–7.
- [29] M. Legrand, C. Pierre, P. Cartraud, J.P. Lombard, Two-dimensional modeling of an aircraft engine structural bladed disk-casing modal interaction, *J. Sound Vib.* 319 (1–2) (2009) 366–391.
- [30] Q. He, H.J. Xuan, L.F. Liao, W.R. Hong, R.R. Wu, Simulation methodology development for rotating blade containment analysis, *J. Zhejiang Univ. Sci. A* 13 (4) (2012) 239–259.
- [31] S. Nitschke, T. Wollmann, C. Ebert, T. Behnisch, A. Langkamp, T. Lang, E. Johann, M. Gude, An advanced experimental method and test rig concept for investigating the dynamic blade-tip/casing interactions under engine-like mechanical conditions, *Wear* 422 (2019) 161–166.
- [32] F.F. Wei, Y.Y. Chen, Z.Q. Wu, L.L. Chen, J. Meng, Failure analysis of rubbing of the fan tip and case of an engine, *Proc. Eng.* 99 (2015) 1289–1296.
- [33] Q. He, H.J. Xuan, L.L. Liu, W.R. Hong, R.R. Wu, Perforation of aero-engine fan casing by a single rotating blade, *Aerosp. Sci. Technol.* 25 (1) (2013) 234–241.
- [34] Q. He, Z. Xie, H.J. Xuan, L.L. Liu, W.R. Hong, Multi-blade effects on aero-engine blade containment, *Aerosp. Sci. Technol.* 49 (2016) 101–111.
- [35] C.E. Bai, H.J. Xuan, Z.K. He, Y.S. Zou, G. Tang, J. Tang, Research on centrifugal compressor disk containment of auxiliary power unit, *Aerosp. Sci. Technol.* 68 (2017) 37–45.
- [36] M. Legrand, C. Pierre, B. Peseux, Structural modal interaction of a four degree-of-freedom bladed disk and casing model, *J. Comput. Nonlinear Dyn.* 5 (4) (2010) 041013.
- [37] S. Nitschke, A. Batailly, M. Legrand, Two-dimensional modeling of unilateral contact-induced shaft precessional motions in bladed-disk/casing systems, *Int. J. Non-Linear Mech.* 78 (2016) 90–104.
- [38] A. Batailly, M. Legrand, P. Cartraud, C. Pierre, Assessment of reduced models for the detection of modal interaction through rotor stator contacts, *J. Sound Vib.* 329 (26) (2010) 5546–5562.
- [39] E.P. Petrov, Multiharmonic analysis of nonlinear whole engine dynamics with bladed disc-casing rubbing contacts, in: *ASME Turbo Expo 2012: Turbine Technical Conference and Exposition*, 2012 June 11–15, Copenhagen, Denmark, ASME, New York, 2012, pp. 1–11.
- [40] J. Hong, T.R. Li, Z.C. Liang, D.Y. Zhang, Y.H. Ma, Research on blade-casing rub-impact mechanism by experiment and simulation in aeroengines, *Shock Vib.* 2019 (2019) 1–15.
- [41] Y. Liu, J.Y. Han, Z.Y. Xue, Y. Zhang, Q. Yang, Structural vibrations and acoustic radiation of blade-shafting-shell coupled system, *J. Sound Vib.* 463 (2019) 1–18.
- [42] H. Ma, F.L. Yin, Z.Y. Wu, X.Y. Tai, B.C. Wen, Nonlinear vibration response analysis of a rotor-blade system with blade-tip rubbing, *Nonlinear Dyn.* 84 (3) (2016) 1225–1258.
- [43] F. Thiery, R. Gustavsson, J.O. Aidanpää, Dynamics of a misaligned Kaplan turbine with blade-to-stator contacts, *Int. J. Mech. Sci.* 99 (2015) 251–261.
- [44] C. Wang, D.Y. Zhang, Y.H. Ma, Z.C. Liang, J. Hong, Dynamic behavior of aero-engine rotor with fusing design suffering blade off, *Chin. J. Aeronaut.* 30 (3) (2017) 918–931.
- [45] S.K. Sinha, Rotordynamic analysis of asymmetric turbofan rotor due to fan blade-loss event with contact-impact rub loads, *J. Sound Vib.* 332 (9) (2013) 2253–2283.
- [46] J. Zeng, H. Ma, X.X. Ma, Z.Y. Wu, Z.Y. Qin, Blade-loss-caused rubbing dynamic characteristics of rotor-bladed disk-casing system, *Trans. Nanjing Univ. Aeronaut. Astronaut.* 35 (1) (2018) 116–125.
- [47] G. Chen, Simulation of casing vibration resulting from blade-casing rubbing and its verifications, *J. Sound Vib.* 361 (2016) 190–209.
- [48] P.C. Yu, D.Y. Zhang, Y.H. Ma, J. Hong, Dynamic modeling and vibration characteristics analysis of the aero-engine dual-rotor system with Fan blade out, *Mech. Syst. Signal Process.* 106 (2018) 158–175.
- [49] H.F. Wang, G. Chen, P.P. Song, Simulation analysis of casing vibration response and its verification under blade-casing rubbing fault, *J. Vib. Acoust.* 138 (3) (2016) 1–14.
- [50] M. Parent, F. Thouverez, F. Chevillot, 3D interaction in bladed rotor-to-stator contact, in: *Proceedings of EURO-DYN 9th International Conference on Structural Dynamics*, 2014 June 30–July 2, Porto, Portugal, 2014, pp. 2035–2042.
- [51] N.F. Wang, C. Liu, D.X. Jiang, B. Kamran, Casing vibration response prediction of dual-rotor-blade-casing system with blade-casing rubbing, *Mech. Syst. Signal Process.* 118 (2019) 61–77.
- [52] M.O. Parent, F. Thouverez, Phenomenological model for stability analysis of bladed rotor-to-stator contacts, in: *International Symposium on Transport Phenomena and Dynamics of Rotating Machinery*, 2016 April, Honolulu, United States, 2016, pp. 1–13.

